Chinese Chemical Letters 33 (2022) 470–474

Contents lists available at ScienceDirect

Chinese Chemical Letters

journal homepage: www.elsevier.com/locate/cclet

$SbPS_4$: A novel anode for high-performance sodium-ion batteries

Miao Yang[a,b,1], Zhonghui Sun[c,1], Ping Nie[d], Haiyue Yu[b], Chende Zhao[b], Mengxuan Yu[b], Zhongzhen Luo[e,*], Hongbo Geng[a,*], Xinglong Wu[b,f,**]

[a] School of Materials Engineering, Changshu Institute of Technology, Changshu 215500, China
[b] Faculty of Chemistry, Northeast Normal University, Changchun 130024, China
[c] Center for Advanced Analytical Science, School of Chemistry and Chemical Engineering, Guangzhou University, Guangzhou 510006, China
[d] Key Laboratory of Preparation and Application of Environmental Friendly Materials (Jilin Normal University), Ministry of Education, Changchun 130103, China
[e] Key Laboratory of Eco-materials Advanced Technology, College of Materials Science and Engineering, Fuzhou University, Fuzhou 350108, China
[f] Key Laboratory for UV Light-Emitting Materials and Technology, Northeast Normal University, Ministry of Education, Changchun 130024, China

ARTICLE INFO

Article history:
Received 1 June 2021
Revised 13 June 2021
Accepted 23 June 2021
Available online 30 June 2021

Keywords:
Sodium-ion batteries
High-capacity anode
Thiophosphate
$SbPS_4$/GO
Full cell

ABSTRACT

With the in-depth research of sodium-ion batteries (SIBs), the development of novel sodium-ion anode material has become a top priority. In this work, tube cluster-shaped $SbPS_4$ was synthesized by a high-temperature solid phase reaction. Then the typical short tubular ternary thiophosphate $SbPS_4$ compounded with graphene oxide ($SbPS_4$/GO) was successfully synthesized after ultrasonication and freeze-drying. $SbPS_4$ shows a high theoretical specific capacity (1335 mAh/g) according to the conversion-alloying dual mechanisms. The unique short tube inserted in the spongy graphene structure of $SbPS_4$/GO results in boosting the Na ions transport and alleviating the huge volume change in the charging and discharging processes, improving the sodium storage performance. Consequently, the tubular $SbPS_4$ compounded with 10% GO provides an outstanding capacity of 359.58 mAh/g at 500 mA/g. The result indicates that $SbPS_4$/GO anode has a promising application potential for SIBs.

Recently, due to the fluctuation of fossil energy prices, global warming caused by the destruction of ecosystems, and fossil fuels are gradually drying up. Researchers have conducted a lot of work in the development of sustainable energy [1]. Solar energy, wind energy, and tidal energy stand out owing to their renewability, but there are many limitations in actual commercial applications [2]. Therefore, it is particularly important to use cheap, efficient and safe equipment to store the generated energy. Among the numerous energy storage systems, lithium-ion batteries (LIBs) are well developed with the advantages of light density, small size and high energy density. Also, LIBs have been widely applied in many commercial fields, from small digital products to automobiles [3]. However, there have obvious shortcomings of LIBs, such as the scarce resources and uneven distribution of lithium salts in the earth's crust. With the large-scale commercial application of LIBs, the price of lithium resources rises quickly, which significantly limits the applicability of LIBs in stationary energy storage [4–6]. Therefore, sodium-ion, potassium-ion batteries [7] and aqueous zinc-ion batteries [8] have gradually developed.

Sodium-ion batteries (SIBs) have become a promising candidate to LIBs owing to the similar electrochemical reaction mechanism [9]. In terms of material cost, the high abundance of sodium-based resources makes it indisputable have an advantage over lithium-based materials. However, Na^+/Na couple has higher redox potential than that of Li^+/Li. Due to the large mass and atomic radius of sodium, the energy density of SIBs is low and their cycling performance is poor [10–12]. Therefore, it is significant to find more suitable electrode materials [13], especially anode materials [14]. An ideal anode material should have the advantages of economy, high-capacity storage property, good rate capability and low reaction potential [15]. The electrode materials based on conversion reaction mechanism, especially the metal sulfides and phosphides [16] are the promising anode materials of SIBs. However, their drastic volume expansion and chemical instability seriously impede the rate and cycling performance, limiting their practical application. Because of the high theoretical specific capacity and relatively low redox potential, alloy anodes have attracted much attention for SIBs. At present, the research hotspots of alloy an-

* Corresponding authors.
** Corresponding author at: Faculty of Chemistry, Northeast Normal University, Changchun 130024, China.
E-mail addresses: zzluo@fzu.edu.cn (Z. Luo), hbgeng@cslg.edu.cn (H. Geng), xinglong@nenu.edu.cn (X. Wu).
[1] These authors contributed equally to this work.

https://doi.org/10.1016/j.cclet.2021.06.065
1001-8417/

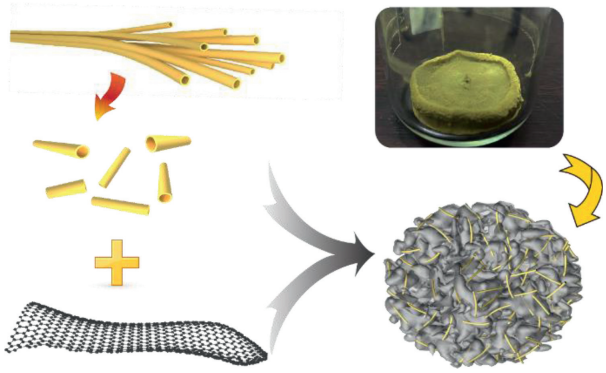

Scheme 1. The synthesis process of $SbPS_4$/GO composite.

odes mainly include the following two elements, Sn and Sb [17,18]. But there is a serious problem in both of them. As the charge and discharge processes proceed, the electrode materials undergo huge volume change, which lead to the cracking of the electrode materials and the deterioration of battery cycling stability. Therefore, exploring novel anode materials with excellent electrochemical performance is urgently needed for practical applications.

Thiophosphate has come into the field of researchers due to its high conductivity and low Vander Waals force. It is widely used in supercapacitors, photocatalysts, and electrocatalysts [19,20]. However, when used as electrode material, due to the presence of phosphorus and sulfur, it is accompanied by drastic volume change during cycling process. Therefore, alleviating volume change based on its excellent electrochemical performance is the top priority of current research. Among them, the modification of the material itself and the coating of carbon materials are considered effective methods. In this work, we use $SbPS_4$ as an anode for SIBs [21]. Due to the combination of alloying and conversion mechanisms, the theoretical specific capacity of $SbPS_4$ is 1335 mAh/g. In order to alleviate its volume effect, the tube cluster $SbPS_4$ is fragmented to form the short tube and composited with graphene oxide (GO). When used as an anode of SIBs, a splendid reversible capacity of 772.2 mAh/g was obtained at 0.1 A/g. While further improving the current density to 5 A/g, a charge capacity of 360 mAh/g has remained. When it returns original current density, the $SbPS_4$/GO can obtain a capacity of 637.33 mAh/g, proving the structural stability of the $SbPS_4$/GO at a high rate. The resultant $SbPS_4$/GO is considered to improve the electron/Na^+ transport and relieve the volume change during charging/discharging process. The $SbPS_4$/GO material displays high competitiveness in comparison with binary metal sulfides and phosphides for SIBs.

Scheme 1 shows the detailed preparation process of $SbPS_4$/GO. Firstly, the tube cluster $SbPS_4$ is synthesized by the high-temperature calcination method. After that, $SbPS_4$ is transformed into a short tube by fragmentation. Lastly, $SbPS_4$/GO is obtained by composite with GO and freeze-drying. During the preparation process, the short tubular $SbPS_4$ is embedded in the spongy GO. Through the addition of GO, the conductivity of the material can be improved, the transmission distance of sodium ions and electrons can also be shortened, and the volume expansion during charging and discharging can be alleviated, resulting in the improvement of the electrochemical performance. The chemical composition and structure of the product are discussed in detail in Fig. 1a, and the diffraction peaks of $SbPS_4$ prepared by high-temperature calcination are well matched. The diffraction peak intensity of $SbPS_4$ decreased after adding GO, which was due to the reduction of the size of $SbPS_4$ and the compound of carbon. Raman results on $SbPS_4$/GO and GO show that the intensity ratio of D-band and G-band (I_D/I_G) of the two samples are 1.01 and 0.98, respectively

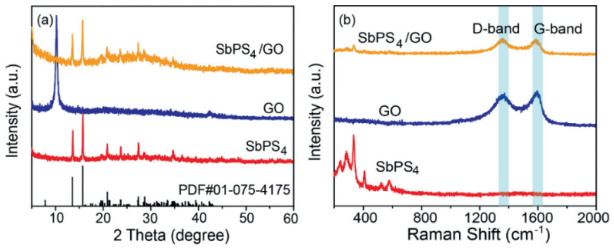

Fig. 1. The structural characterizations of $SbPS_4$/GO: (a) XRD patterns, (b) Raman spectra.

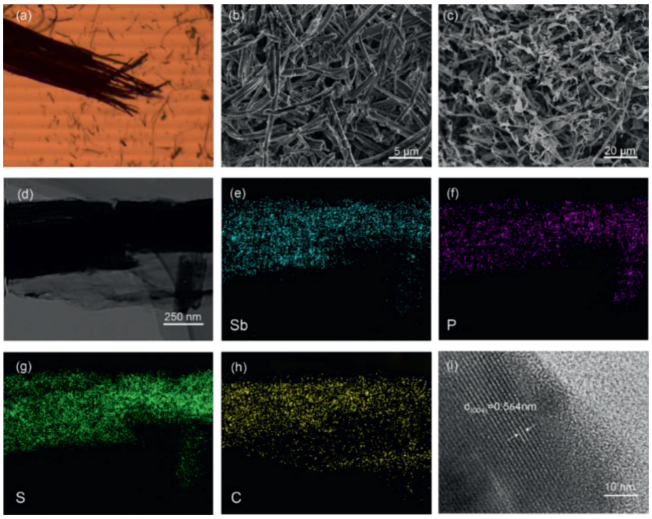

Fig. 2. (a) Upright metallographic microscope image of tube cluster $SbPS_4$. SEM images of (b) $SbPS_4$ after fragmentation and (c) $SbPS_4$/GO. TEM image of (d) $SbPS_4$/GO and elemental mapping of (e-h) $SbPS_4$GO. (i) HRTEM image of $SbPS_4$/GO.

(Fig. 1b). The higher I_D/I_G ratio indicates the amorphous state of the carbonaceous materials owing to the porous feature [22].

Tube cluster $SbPS_4$ can be clearly observed in the upright metallurgical microscope image (Fig. 2a). After fragmenting, its original tubules remain almost intact, and the size of each unit is significantly reduced (Fig. 2b). As displayed in the SEM image (Fig. 2c), GO glues together the nanosized short tubes of $SbPS_4$ to form a continuous conductive network that can significantly promote electron transfer. In addition, due to the presence of spongy graphene, there are obvious pore channels to guarantee the electrolyte complete penetration and the rapid ions migration. $SbPS_4$/GO has a large number of pore channels, which can also be determined through the pore size distribution diagram (Fig. S1 in Supporting information). The element mappings of $SbPS_4$/GO in Figs. 2d–h confirm the uniform distribution of Sb, P, S and C, which is consistent with the SEM image shown in Fig. S2 (Supporting information). The lattice spacing of 0.564 nm in the HRTEM image coincides with the (004) plane of the crystal $SbPS_4$ (Fig. 2i), indicating the good purity of $SbPS_4$.

Fig. 3a shows the discharge/charge profiles of $SbPS_4$, $SbPS_4$-X45 and $SbPS_4$/GO composite in the initial five cycles. $SbPS_4$-X45 was selected as the comparison material because it has the best electrochemical performance as shown in Fig. S3 (Supporting information). $SbPS_4$ composited with 10% GO has the highest ionic conductivity and the lowest resistance value (Fig. S4 in Supporting information). The specific capacities of $SbPS_4$, $SbPS_4$-X45, and $SbPS_4$/GO at 0.1 A/g are 356.6, 717.2 and 772.71 mAh/g, respectively. The improved electrochemical performance of $SbPS_4$/GO is ascribed to the nanominiaturization of tubular materials and the appropriate amount of composite with carbon materials (GO).

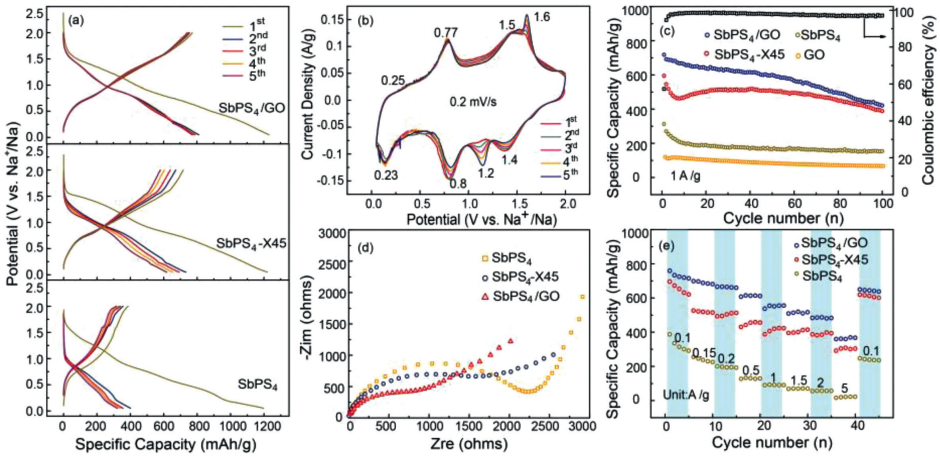

Fig. 3. (a) Galvanostatic curves of $SbPS_4$, $SbPS_4$-X45, $SbPS_4$/GO at 0.1 A/g for the initial five cycles. (b) CV profiles of $SbPS_4$/GO for the five cycles at 0.2 mV/s. (c) Long cycling performance of $SbPS_4$, $SbPS_4$-X45, $SbPS_4$/GO and corresponding Coulombic efficiency at 1 A/g. (d) Nyquist plots. (e) Rate performance at various current densities.

The electrochemical properties of $SbPS_4$/GO are studied by the CV tests at a sweep rate of 0.2 mV/s (Fig. 3b). At the first cathodic process, a peak located at 1.4 V can be indexed as the intercalation of Na^+ into the $SbPS_4$/GO, while the distinct peak near 1.2 V is attributed to the conversion reaction of Na_2S. The peak at 0.8 V corresponds to the breaking of P-S bond and the production of Na_3P and Sb, while the peak at 0.23 V ascribes to the production of Na_3Sb [23]. During the initial anodic scan, the weak broad peak located at 0.25 V indicates Na_3P desodiation, and the peak at 0.77 V attributed to Na_3Sb dealloying. The next 1.5 V and 1.6 V peaks ascribe to Na_2S and Na^+ further desodiation reaction [24]. Remarkably, the CV profiles remain almost overlapped, suggesting the excellent electrochemical reversibility. Therefore, the corresponding redox reactions mechanism of $SbPS_4$ can be listed as follows:

$$SbPS_4 + 14Na^+ + 14e^- \rightarrow Na_3Sb + 4Na_2S + Na_3P$$

$$Na_3P \leftrightarrow 3Na^+ + 3e^- + P$$

$$Na_3Sb \leftrightarrow 3Na^+ + 3e^- + Sb$$

$$Na_2S \leftrightarrow 2Na^+ + 2e^- + S$$

Fig. 3c shows the cycling performance of different samples at 1 A/g. The reversible capacity of $SbPS_4$/GO is 420.52 mAh/g after 100 cycles with the initial coulombic efficiency of 57%, which is superior to $SbPS_4$–X45 and $SbPS_4$. The Nyquist plots of the three samples consist of a depressed semicircle at the high frequency corresponding to the charge transfer process and an oblique line at the low frequency corresponding to the charge transfer process and an oblique line at the low frequency representing Na^+ diffusion process, confirming a faster electronic and ionic transport of $SbPS_4$/GO than that of $SbPS_4$-X45 and bare $SbPS_4$ (Fig. 3d). The EIS plots of materials with different mixed graphene content are shown in Fig. S5a (Supporting information). It can be seen that $SbPS_4$ composited with 10% GO has the smallest resistance value. As expected, it exhibits the best electrochemical performance, which is consistent with the data shown in Fig. S4. The EIS analysis in Fig. S5b (Supporting information) shows that the charge transfer resistance (R_{ct}) of the 100th cycle is lower than that of before cycling state, which may be due to the formation of the stable SEI layer between the electrode material and the electrolyte after repeated cycles, which is conducive to the transport of Na^+. As shown in Fig. 3e, the $SbPS_4$/GO has the capacity of 359.58 mAh/g at 5 A/g. Importantly, the capacity of $SbPS_4$/GO can return to 637.33 mAh/g when the current density returns to 0.1 A/g, indicating the structural stability of $SbPS_4$/GO at a high rate.

To further explore the possible reaction mechanism during the Na-insertion/extraction process, *ex situ* XRD and XPS analysis of

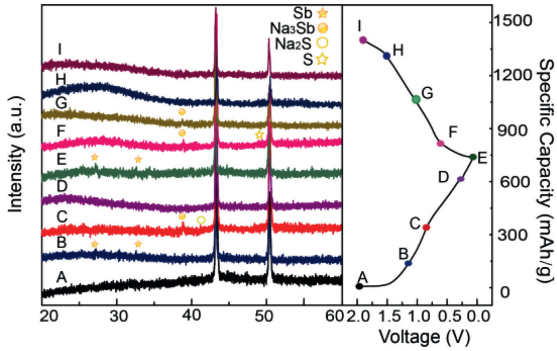

Fig. 4. *Ex situ* XRD patterns of $SbPS_4$/GO taken at different stages at 1 A/g.

$SbPS_4$/GO were performed at specific distinct potentials of the first charge/discharge curve. As shown in Fig. 4, when the cell was discharged to 1.3 V, the Na_2S was found [25]. The presence of Na_2S reveals that sodium ions react with sulfur after insertion into $SbPS_4$. When the discharge voltage reaches 0.9 V, the characteristic peak of Sb has appeared. Further discharging to 0.3 V, Na_3Sb was detected. After it was discharged to 0.05 V, the diffraction peak of Na_3Sb becomes stronger and Na_2S still exists. In the charging process, the diffraction peak of Sb appears again when the cell was charged to 1.0 V. With the extraction of sodium ions, the diffraction peaks of Na_3Sb and S indicated that the desodiation reaction of Na_2S and the dealloying process are not completed [26]. After charging to 2 V, the signal of Na_3Sb almost disappears. Compared with the original state, the diffraction peaks of fully charged state hardly change, further confirming the excellent reversibility of the $SbPS_4$/GO.

XPS studies of the electrodes were carried out at various discharge/charge states in the first cycle. Fig. 5 shows the high-resolution S 2p and P 2p spectra of $SbPS_4$/GO electrode with the SnP_2S_6 and Cu_3PS_4 as the references. In Fig. 5a, the peaks corresponding to the S $2p_{3/2}$ and S $2p_{1/2}$ signals at 161.6 and 162.8 eV can be assigned to Na_2S [27]. The binding energy of 168.8 eV corresponds to S. It indicates that Na_2S and S exist in the whole charge and discharge processes. Both the peak intensities of Na_2S and S increase during the discharge process [28]. There is still a tiny amount of Na_2S and S at the end of the charging stage, indicating that the transformation reaction of S is not completely reversible. In Fig. 5b, the two splitting peaks located at 132.6 and

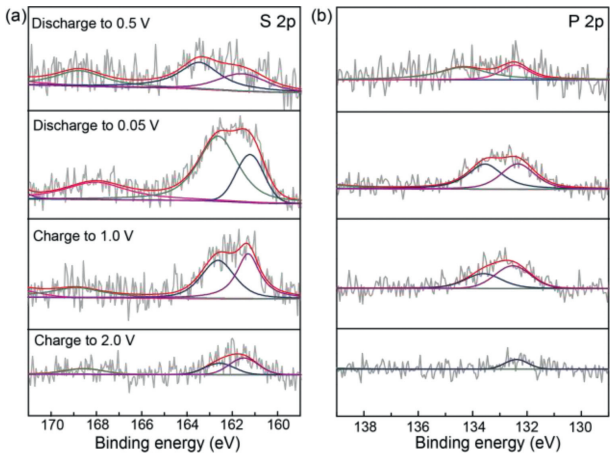

Fig. 5. XPS analysis of the S 2p and P 2p signal for the electrodes at selected potentials in the first cycle.

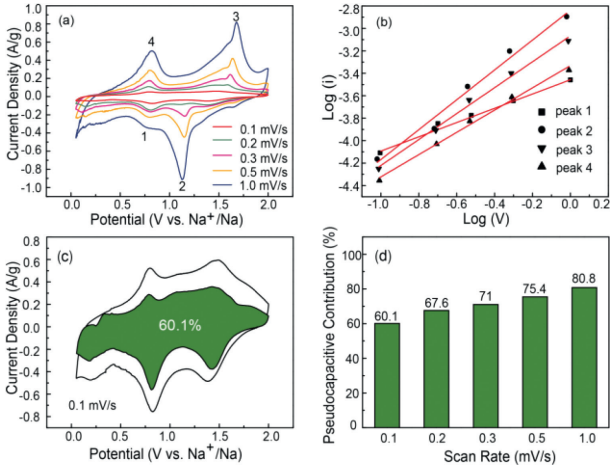

Fig. 6. (a) CV curves at diverse sweep rates. (b) Linear relationship of log(i) *vs.* log(v). (c) Proportion of capacitive (shaded region) contribution at 0.1 mV/s. (d) Contribution percentage of capacitive and diffusion-controlled capacities *vs.* scan rates.

133.7 eV were ascribed as the P-S bonding and $2p_{1/2}$ of the P 2p spectrum, respectively [29]. It can be seen that P elemental substance increases with the discharge process. Upon charging, the amount of P is gradually decreased with forming P-S bonding. As shown in Fig. S6a (Supporting information), the Sb 3d spectrum overlaps with O 1s spectrum and shows two peaks at 531 and 539.8 eV, which are attributed to the presence of Sb $3d_{3/2}$ [30]. In addition, 535 and 532.5 eV correspond to the presence of O–C and O = C functional group, respectively [31]. It can be seen from Fig. S6 (Supporting information) that a large amount of Sb is generated as discharged to 0.5 V. With further discharging to 0.05 V, the amount of Sb decreases due to the occurrence of alloying reaction. When charged to 1.0 V, the dealloying of Na_3Sb leads to an increase of Sb content. In the end, the charging is completed to 2.0 V, Sb still exists but the amount becomes less. In the C 1s spectrum of Fig. S6b, the peaks at 287.7 eV, 285.5 eV and 284.3 eV can be ascribed to O–C=O, C–O and C–C bonds, respectively.

To reveal the origin of high rate performance of $SbPS_4$/GO, the sodium storage mechanism was studied by analyzing CV profiles at various scan rates from 0.1 mV/s to 1.0 mV/s (Fig. 6a). The charge storage mechanism of $SbPS_4$/GO can be quantified by dividing the current (i) at a fixed potential (v) into two mechanisms: k_1v and $k_2v^{0.5}$. Here, a and b are adjustable parameters, v is scan rate, and

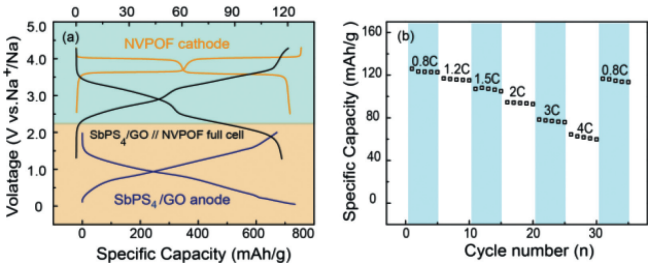

Fig. 7. (a) Initial charge/discharge profiles of the full-cell and the homemade NVPOF cathode and $SbPS_4$/GO anode in the half-cell. (b) Rate capability of the full-cell at different rates.

k_1 and k_2 are constants.

$$i = av^b$$

$$\log(i) = b \times log(v) + log(a)$$

$$i = k_1v + k_2v^{0.5}$$

If the b value approaches to 1, the electrochemical process is a surface-controlled process, such as adsorption/resolution [32]. When the b value is 0.5, the process mainly relies on the diffusion-controlled process [33]. Fig. 6b shows the fitting results of log(i) to log(v). The values of b are 0.64, 1.37, 1.16 and 0.98, respectively. With the increase of scanning rate, the reaction of sodium ions is similar to the adsorption-desorption process, resulting in peak 2 being a surface-controlled process, and the same mechanism exists at peak 3 [34]. Fig. 6c shows the normalized contribution percentage of capacitive and diffusion-controlled capacities. When the scanning rate is 0.1 mV/s, the capacitive contribution ratio reaches 60.1%. The contribution rate of *pseudo*-capacitance is predominant with the increase of current density as shown in Fig. 6d. The results indicate that pseudo-capacitance plays a decisive role in Na-ion storage at high scan rates, thus resulting in excellent rate capability [35].

Motivated by such a superior specific capacity and an excellent rate capability of the $SbPS_4$/GO anode. Na-ion full cell was constructed by coupling with $Na_3V_2O_2(PO_4)_2F$ (NVOPF) cathode for practical applications [36]. The NVOPF cathode exhibits a high discharge capacity of ~120 mAh/g at 0.1 C in a half-cell configuration. The typical charge/discharge curve of the Na-ion full cell shows an outstanding specific capacity of 119 mAh/g at 0.8 C between 1.2 V and 4.3 V (based on the weight of cathode) (Fig. 7a). The full cell possesses two discharge plateaus located at 3.8–3.0 V and 2.5–1.8 V, respectively. Moreover, the specific capacity of 63 mAh/g could be obtained at 4 C (Fig. 7b), indicating the superior rate capability of the Na-ion full cell. Furthermore, the full cell shows 62% capacity retention in comparison of the first cycle, exhibiting good cycling performance (Fig. S7 in Supporting information). Such a superior full cell performance indicates the potential application of $SbPS_4$/GO anode for SIBs.

In summary, the $SbPS_4$/GO composite has been intensively studied as anode material for SIBs in this work. The unique structure boosts rapid reaction kinetics, inhibits electrode structural failure and agglomeration for volume change, suppresses the polysulfides shuttle behavior, resulting in excellent rate capability and good cycling performance. As an anode material for the half-cell, the $SbPS_4$/GO exhibits a specific capacity of 772 mAh/g at 0.1 A/g. Moreover, a high capacity of 420.5 mAh/g could be also maintained after 100 cycles (1 A/g). Significantly, it has a high Na ion storage capacity of 119 mAh/g at 0.8 C in the full-cell configuration. The favorable advantages including low-cost composition, facile synthesis process, and excellent electrochemical performance enable the

$SbPS_4$/GO to be a potential anode material for high performance SIBs.

Declaration of competing interest

The authors declare that they have no known competing financial interests or personal relationships that could have appeared to influence the work reported in this paper.

Acknowledgments

We gratefully acknowledge the financial support from the National Natural Science Foundation of China (Nos. 91963118, 51801030). This study is also supported by the Open Project Program of Key Laboratory of Preparation and Application of Environmental Friendly Materials (Jilin Normal University, No. 2020004).

Supplementary materials

Supplementary material associated with this article can be found, in the online version, at doi:10.1016/j.cclet.2021.06.065.

References

[1] Y. Wu, C. Zhang, H. Zhao, Y. Lei, J. Mater. Chem. A 9 (2021) 9506–9534.
[2] T.G. Allen, J. Bullock, X. Yang, A. Javey, S. De Wolf, Nat. Energy 4 (2019) 914–928.
[3] J. Ding, W. Hu, E. Paek, D. Mitlin, Chem. Rev. 118 (2018) 6457–6498.
[4] Y. Li, Y. Lu, C. Zhao, et al., Energy Storage Mater. 7 (2017) 130–151.
[5] M. Yang, Q. Ning, C. Fan, X.L. Wu, Chin. Chem. Lett. 32 (2021) 895–899.
[6] W.H. Li, H.J. Liang, X.K. Hou, et al., J. Energy Chem. 50 (2020) 416–423.
[7] H. Huang, X. Luo, Y. Yao, et al., InfoMat 3 (2021) 421–431.
[8] Y. Heng, Z. Gu, J. Guo, X. Wu, Acta Phys. Chim. Sin. 37 (2021) 2005013.
[9] S. Geng, T. Zhou, M. Jia, et al., Energy Environ. Sci. 14 (2021) 3184–3193.
[10] V. Palomares, M. Casas-Cabanas, E. Castillo-Martínez, M.H. Han, T. Rojo, Energy Environ. Sci. 6 (2013) 2312–2337.
[11] H. Pan, Y.S. Hu, L. Chen, Energy Environ. Sci. 6 (2013) 2338–2360.
[12] X. Hou, W. Li, Y. Wang, et al., Chin. Chem. Lett. 31 (2020) 2314–2318.
[13] Z.Y. Gu, J.Z. Guo, X.X. Zhao, et al., InfoMat 3 (2021) 694–704.
[14] Y. Jiang, Y. Wang, J. Ni, L. Li, InfoMat 3 (2021) 339–352.
[15] H.J. Liang, B.H. Hou, W.H. Li, et al., Energy Environ. Sci. 12 (2019) 3575–3584.
[16] S. Haghighat-Shishavan, M. Nazarian-Samani, M. Nazarian-Samani, K.B. Kim, Energy Storage Mater. 39 (2021) 96–107.
[17] K.T. Chen, S. Chong, L. Yuan, Y.C. Yang, H.Y. Tuan, Energy Storage Mater. 39 (2021) 239–249.
[18] B. Dou, J. Yan, Q. Chen, et al., Sens. Actuator. B. Chem. 328 (2021) 129082.
[19] A. Kato, H. Kowada, M. Deguchi, et al., Solid State Ionics 322 (2018) 1–4.
[20] A. Qiao, H. Tao, Y. Yue, J. Non-Cryst. Solid 521 (2019) 119476.
[21] C.D. Malliakas, M.G. Kanatzidis, J. Am. Chem. Soc. 128 (2006) 6538–6539.
[22] H.J. Liang, Z.Y. Gu, X.Y. Zheng, et al., J. Energy Chem. 59 (2021) 589–598.
[23] Z. Yi, N. Lin, W. Zhang, et al., Nanoscale 10 (2018) 13236–13241.
[24] L. Yang, W. Hong, Y. Tian, et al., Chem. Eng. J. 385 (2020) 123838.
[25] C. Kang, S. Zhou, J. Liu, et al., J. Mater. Chem. A 9 (2021) 2152–2160.
[26] L. Zhou, Z. Cao, J. Zhang, et al., Adv. Mater. 33 (2021) 2005993.
[27] C. Lin, Y. Wang, F. Zhong, et al., Chem. Eng. J. 407 (2021) 126991.
[28] F. Xie, L. Zhang, Q. Gu, et al., Nano Energy 60 (2019) 591–599.
[29] B.H. Hou, Y.Y. Wang, Q.L. Ning, et al., Nanoscale 11 (2019) 1304–1312.
[30] H. Huang, R. Xu, Y. Feng, et al., Adv. Mater. 32 (2020) 1904320.
[31] O.A. Jaramillo-Quintero, R.V. Barrera-Peralta, A.G. El Hachimi, et al., J. Colloid Interface Sci. 585 (2021) 649–659.
[32] H. Lu, F. Ai, Y. Jia, et al., Small 14 (2018) 1802694.
[33] A. Xu, C. Huang, G. Li, et al., J. Mater. Chem. A 9 (20) (2021) 12169–12178.
[34] B.H. Hou, Y.Y. Wang, Q.L. Ning, et al., Adv. Mater. 31 (2019) 1903125.
[35] H.Y. Yu, H.J. Liang, Z.Y. Gu, et al., Electrochim. Acta 361 (2020) 137041.
[36] X. Li, S. Jiang, S. Li, et al., J. Mater. Chem. A 9 (19) (2021) 11827–11838.